ON THE MINIMUM CORE MASS FOR GIANT PLANET FORMATION AT WIDE SEPARATIONS

Ana-Maria A. Piso
Harvard-Smithsonian Center for Astrophysics, 60 Garden Street, Cambridge, MA 02138

Andrew N. Youdin
JILA, University of Colorado and NIST, 440 UCB, Boulder, CO 80309-0440
Draft version October 30, 2013

ABSTRACT

In the core accretion hypothesis, giant planets form by gas accretion onto solid protoplanetary cores. The minimum (or critical) core mass to form a gas giant is typically quoted as $10 M_\oplus$. The actual value depends on several factors: the location in the protoplanetary disk, atmospheric opacity, and the accretion rate of solids. Motivated by ongoing direct imaging searches for giant planets, this study investigates core mass requirements in the outer disk. To determine the fastest allowed rates of gas accretion, we consider solid cores that no longer accrete planetesimals, as this would heat the gaseous envelope. Our spherical, two-layer atmospheric cooling model includes an inner convective region and an outer radiative zone that matches onto the disk. We determine the minimum core mass for a giant planet to form within a typical disk lifetime of 3 Myr. The minimum core mass declines with disk radius, from $\sim 8.5 M_\oplus$ at 5 AU to $\sim 3.5 M_\oplus$ at 100 AU, with standard dust opacities. Lower temperatures in the outer disk explain this trend, while variations in disk density are less influential. At all distances, a lower dust opacity or higher mean molecular weight reduces the critical core mass. Our non-self-gravitating, analytic cooling model reveals that self-gravity significantly affects early atmospheric evolution, starting when the atmosphere is only $\sim 10\%$ as massive as the core.

1. INTRODUCTION

Models of giant planet formation fall in two categories: core accretion or gravitational instability (D'Angelo et al. 2011; Youdin & Kenyon 2013). In core accretion models, a solid core grows until it becomes massive enough to rapidly accrete gas (Perri & Cameron 1974; Mizuno et al. 1978). Gravitational instability (GI) theories investigate the fragmentation of the protoplanetary disk into bound clumps (Cameron 1978; Boss 1997).

Forming giant planets at wide separations in the protoplanetary disk poses theoretical challenges for both models. While disks cannot fragment close to their host star, GI is more promising in the outer disk (Matzner & Levin 2005; Rafikov 2005). However, for GI to form planetary mass objects versus brown dwarfs, both instantaneous disk conditions and the history of gas infall must be finely tuned (Kratter et al. 2010). The main concern for core accretion models, which are successful in the inner disk, is that they operate too slowly in the outer disk. The few Myr lifetime of gas disks sets the constraint (Williams & Cieza 2011). However, mechanisms for the rapid accretion of solids, even at large separations, exist (Dones & Tremaine 1993; Kenyon & Bromley 2009; Lambrechts & Johansen 2012). We thus consider the complementary problem of gas accretion timescales in the outer disk.

Core accretion models fall in several categories: static, quasi-static evolutionary and hydrodynamic. In static models, the accretion of planetesimals provides a steady luminosity that determines the structure and mass of the atmosphere (Stevenson 1982). For a given planetesimal accretion rate, static solutions only exist up to a maximum core mass, referred to as the "critical core mass", $M_{\rm crit}$. Above this mass, the atmosphere is assumed to collapse and rapidly accrete disk gas, a process known as the "core accretion instability."

Many static studies reproduce a canonical $M_{\rm crit} \sim 10 M_\oplus$. However, Rafikov (2011, 2006, hereafter R06) finds a wide range of values, $0.1 M_\oplus \lesssim M_{\rm crit} \lesssim 100 M_\oplus$, depending on the planetesimal accretion rate and disk parameters. Section 6.4 compares our results to R06. A general limitation of static models is the neglect of heat generated by atmospheric collapse, which can transform the core accretion instability into a slower process of Kelvin-Helmholtz (KH) contraction.

Quasi-static models include time-dependent atmospheric evolution due to KH contraction, and typically include a time-varying planetesimal accretion rate (Bodenheimer & Pollack 1986; Alibert et al. 2005). Successful quasi-static models describe three phases of giant planet formation (Pollack et al. 1996). In phase 1, rapid planetesimal accretion gives significant core growth, but prevents the accretion of a massive atmosphere. When planetesimal accretion abates, as the core's feeding zone is depleted of solids, phase 2 begins. During phase 2, the atmosphere grows gradually, cooling by KH contraction. An ongoing trickle of planetesimal accretion can heat the atmosphere and slow this contraction. Eventually, the atmosphere reaches the "crossover mass", when it equals the mass of the now slowly growing core. Phase 3, the runaway growth of the atmosphere, begins around the crossover mass. This runaway occurs quasi-statically, i.e. in hydrostatic balance, but very rapidly compared to disk lifetimes.

Dynamical models are needed to understand how runaway growth ends and final planet masses are determined. Relevant processes – including gap opening in disks and the transition of accretion from spherical to planar – can be simulated and then added to atmospheric

evolution calculations (Lissauer et al. 2009).

This work develops quasi-static models in which the core has a fixed mass and is no longer accreting solids. By isolating the process of KH contraction, we determine the minimum timescale for runaway atmospheric growth, and thus for giant planet formation by core accretion. Previous studies have considered this type of growth (Ikoma et al. 2000; Papaloizou & Nelson 2005), which is an end-member case of phases 2 and 3 in more detailed quasi-static models. Especially since phase 2 atmospheric growth is often the slowest stage of core accretion, understanding the fastest allowed rates of gas accretion is of crucial importance. Our study develops simplified cooling models for the purposes of broadly exploring parameter space – especially in the outer disk – and developing a more detailed understanding of atmospheric accretion.

This paper is organized as follows. Section §2 describes our model of atmospheric growth. In Section §3, we develop a simplified analytic version of our atmospheric model. We describe the structure and evolution of our atmosphere solutions in Section §4. Section §5 gives our final results for growth timescales and critical core masses. We discuss some neglected effects in Section §6 and summarize our findings in Section §7. Some detailed derivations are presented in the appendices.

2. ATMOSPHERIC ACCRETION MODEL

To model the accretion of gas by a solid protoplanet, we develop a simplified two-layer model for time-dependent atmospheric growth via cooling, i.e. KH contraction. With a convective interior and radiative exterior, this model is motivated by similar models of hot Jupiters (Arras & Bildsten 2006; Youdin & Mitchell 2010).

Our model can treat atmospheric growth up to the early stages of runaway growth, around the crossover mass. At higher masses, our approximate treatment of the radiative zone (explained below) breaks down. Since evolution after the onset of runaway growth contributes minimally to the total planet formation timescale, we can model growth times to good accuracy.

Our main assumptions are summarized as follows:

1. The atmosphere is spherically symmetric, remains in hydrostatic balance, and matches onto the disk's midplane temperature and pressure at the planet's Hill radius.

2. The core mass and radius are fixed in evolutionary calculations, neglecting ongoing planetesimal or dust accretion.

3. Gravitational contraction of the atmosphere is the only source of planetary luminosity.

4. Cooling of the atmosphere is dominated by the convective interior. Thus the luminosity in the radiative exterior is held spatially constant.

5. A polytropic equation of state (EOS) is assumed for simplicity.

6. Dust grains provide the opacity in the radiative zone, which remains cool enough to avoid dust sublimation.

The first assumption of spherical accretion breaks down early in the inner disk, as explained below. However, our focus is the outer disk, where this standard approximation is better justified.

2.1. Disk and Opacity Model

We adopt a minimum mass solar nebula (MMSN) model for a passively irradiated disk (Chiang & Youdin 2010). With the semimajor axis a normalized to the outer disk as $a_{10} = a/(10 \text{ AU})$, the gas surface density and mid-plane temperature are

$$\Sigma_{\rm d} = 70 \, F_\Sigma a_{10}^{-3/2} \text{ g cm}^{-2} \tag{1a}$$

$$T_{\rm d} = 45 \, F_T \, a_{10}^{-3/7} \text{ K}. \tag{1b}$$

The normalization factors F_Σ and F_T adjust the model relative to the fiducial MMSN. We fix $F_\Sigma = F_T = 1$ unless noted otherwise. Some observations support a flatter surface density profile, $\Sigma_{\rm d} \propto a^{-1}$ (Andrews et al. 2010). We find that gas density and pressure are weak corrections to atmospheric growth (see Section §5). However, a greater surface density of solids in the outer disk could favor the rapid growth of cores (Bromley & Kenyon 2011).

For a vertically isothermal disk in hydrostatic balance (with no self-gravity), the mid-plane pressure of disk gas is

$$P_{\rm d} = 6.9 \times 10^{-3} F_\Sigma \sqrt{F_T} \, a_{10}^{-45/14} \text{ dyn cm}^{-2} \tag{2}$$

for a molecular weight of $\mu = 2.35$ proton masses and a Solar mass star.

The (thermodynamically isothermal) sound speed in the disk is

$$c_{\rm d} = \sqrt{\mathcal{R} T_{\rm d}} = 0.4 \sqrt{F_T} a_{10}^{3/14} \text{ km s}^{-1}, \tag{3}$$

in terms of the specific gas constant $\mathcal{R}$. The disk scale height is

$$H_{\rm d} = c_{\rm d}/\Omega = 0.42 \sqrt{F_T} \, a_{10}^{9/7} \text{ AU}, \tag{4}$$

in terms of the Keplerian frequency $\Omega = \sqrt{GM_*/a^3}$, with G the gravitational constant and M_* the stellar (in this work Solar) mass.

We assume a dust opacity characteristic of interstellar grains, following Bell & Lin (1994):

$$\kappa = 2F_\kappa \left(\frac{T}{100 \text{ K}} \right)^\beta \text{ cm}^2 \text{ g}^{-1}, \tag{5}$$

with a power-law index $\beta = 2$ and normalization $F_\kappa = 1$ unless noted otherwise. Grain growth tends to lower both F_κ and β, while dust abundance scales with F_κ. Section §6.2 discusses dust sublimation and more realistic opacity laws.

2.2. Length Scales

The characteristic length scales for protoplanetary atmospheres are crucial for choosing boundary conditions and for understanding the validity of spherical symmetry in a gas disk of scale height $H_{\rm d}$.

The solid core has a radius

$$R_{\rm c} \equiv \left(\frac{3M_{\rm c}}{4\pi\rho_{\rm c}} \right)^{1/3} \approx 10^{-4} m_{\rm c10}^{1/3} \text{ AU}, \tag{6}$$

where the core mass, M_c, is normalized to 10 Earth masses as $m_{c10} \equiv M_c/(10\,M_\oplus)$. The core density is held fixed at $\rho_c = 3.2$ g cm^{-3}, representing a mixture of ice and rocky material (Papaloizou & Terquem 1999). We thus neglect the detailed EOS of the solid core (Fortney et al. 2007).

A planet can bind a dense atmosphere if its escape velocity exceeds the sound speed. This criterion is satisfied inside the Bondi radius

$$R_B \equiv \frac{GM_p}{c_d^2} \approx 0.17\,\frac{m_{p10}\,a_{10}^{3/7}}{F_T}\;\;\text{AU}, \tag{7}$$

where the enclosed planet mass, $M_p = M_c + M_{atm}$, includes the core and any atmosphere within the Bondi radius and $m_{p10} \equiv M_p/(10\,M_\oplus)$. The contribution of the atmospheric mass is small in early evolutionary stages.

Stellar tides dominate the planet's gravity beyond the Hill radius

$$R_H = \left(\frac{M_p}{3M_*}\right)^{1/3} a \approx 0.22\,m_{p10}^{1/3}\,a_{10}\;\;\text{AU}, \tag{8}$$

where hydrostatic balance breaks down. (Here we use the same symbol, M_p, to now mean the mass within R_H.)

The relevant length scales of the atmosphere and disk satisfy the relation $R_B H_d^2 = 3R_H^3$. The length scales are roughly equal at the "thermal mass" (e.g., Menou & Goodman 2004)

$$M_{th} > \frac{c_d^3}{G\Omega} \approx 25\,\frac{F_T^{3/2}}{\sqrt{m_*}}\,a_{10}^{6/7}\;M_\oplus\,. \tag{9}$$

In the low mass regime, $M_p < M_{th}/\sqrt{3}$, the length scales order as $R_B < R_H < H_d$. In this regime, many studies assume the atmosphere matches the disk conditions at R_B. We use R_H as the matching radius in all regimes. We are accounting for the fact that, in hydrostatic models, the density at R_B is higher than the background density (see R06). Nevertheless, since the density change is modest, these two boundary conditions give similar results.

For a finite range of intermediate masses, $M_{th}/\sqrt{3} < M_p < 3M_{th}$, the Hill radius is the smallest scale, satisfying both $R_H < R_B$ and $R_H < H_d$. Spherical symmetry remains a good, if imperfect, approximation because the disk is only weakly vertically stratified on scales $\lesssim H_d$.

At higher planet masses where $M_p > 3M_{th}$ and $H_d < R_H < R_B$, spherical symmetry is no longer a good approximation, due to both the vertical stratification of the disk and gap opening. See §6.1 for further discussion of neglected hydrodynamic effects.

While R_H is always the outer boundary in our structure calculations, we quote planet masses as the enclosed mass within the smaller of R_B and R_H.

2.3. Structure Equations and Boundary Conditions

Our atmosphere calculations use the standard structure equations of mass conservation, hydrostatic balance, thermal gradients, and energy conservation:

$$\frac{dm}{dr} = 4\pi r^2 \rho \tag{10a}$$

$$\frac{dP}{dr} = -\frac{Gm}{r^2}\rho \tag{10b}$$

$$\frac{dT}{dr} = \nabla\frac{T}{P}\frac{dP}{dr} \tag{10c}$$

$$\frac{dL}{dr} = 4\pi r^2 \rho\left(\epsilon - T\frac{\partial S}{\partial t}\bigg|_m\right), \tag{10d}$$

where r is the radial coordinate, L is the luminosity, and P, T, ρ and S are the gas pressure, temperature, density and entropy, respectively. The enclosed mass at radius r is m. Equation (10c) simply defines the temperature gradient $\nabla \equiv d\ln T/d\ln P$.

Radiation diffusion gives a temperature gradient

$$\nabla_{rad} \equiv \frac{3\kappa P}{64\pi Gm\sigma T^4}L\,, \tag{11}$$

with σ the Stefan-Boltzmann constant. In our models, optically thick diffusion is a good approximation throughout the radiative zones. In convectively unstable regions, efficient convection gives an isentropic temperature gradient with $\nabla = \nabla_{ad}$, the adiabatic gradient

$$\nabla_{ad} \equiv \left(\frac{d\ln T}{d\ln P}\right)_{ad}. \tag{12}$$

According to the Schwarzschild criterion, convective instability occurs when $\nabla_{rad} > \nabla_{ad}$. Thus $\nabla = \min(\nabla_{rad}, \nabla_{ad})$ sets the temperature gradient.

In the energy equation (10d), ϵ represents all local sources of heat input, except for the motion of the atmosphere itself. From stellar structure, ϵ may be familiar as a nuclear burning term. In a protoplanetary atmosphere, dissipative drag on planetesimals contributes to ϵ. Our models set $\epsilon = 0$, consistent with our neglect of planetesimal accretion.

The energy input from gravitational contraction, $\epsilon_g = -T\partial S/\partial t$, is crucial for a cooling model.[1] The partial time derivative would normally require our radial derivative to be partial as well. However, our subsequent developments will replace the local energy equation (10d) with global energy balance (see section §2.4), reverting the structure equations to time-independent ordinary differential equations (ODEs).

To solve the equation set (10), an EOS is required for closure. In our study, we adopt an ideal gas law with a polytropic EOS

$$P = \rho\mathcal{R}T\,, \tag{13a}$$

$$S = \mathcal{R}\ln\left(\frac{T^{1/\nabla_{ad}}}{P}\right), \tag{13b}$$

with S a relative entropy. This work uses $\nabla_{ad} = 2/7$, i.e. a polytropic index $\gamma \equiv 1/(1-\nabla_{ad}) = 7/5$, for an ideal diatomic gas.[2] We thus neglect the presence of monatomic Helium in our choice of polytropes, a common practice

---

[1] In general, any motion is accounted for by this term. The partial time derivative is performed on shells of fixed mass.

[2] Equation (13b) is equivalent to the standard polytropic relation, $P = K\rho^\gamma$, if the polytropic index K replaces S.

in idealized studies. We do, however, account for Helium in our reference value of $\mu = 2.35$ proton masses.

Boundary conditions must be satisfied at both the base and the top of the atmosphere, with $m(R_c) = M_c$, $T(R_H) = T_d$ and $P(R_H) = P_d$. Our model atmospheres also obey $L(R_c) = 0$. Along with Equation (10d), this boundary condition is incorporated in the global cooling model described below.

2.4. Global Cooling of an Embedded Planet

We now consider the global energy balance of a planet embedded in a gas disk. More generally, our derivation applies to any spherical, hydrostatic object in pressure equilibrium with a background medium. The total atmospheric energy includes gravitational and internal energies, $E = E_G + U$, with

$$E_G = -\int_{M_c}^{M} \frac{Gm}{r} dm \,, \qquad (14a)$$

$$U = \int_{M_c}^{M} u\, dm \,. \qquad (14b)$$

The specific internal energy is $u = C_V T = \mathcal{R}(\nabla_{ad}^{-1} - 1)T$ for a polytropic EOS. For a star or coreless planet, $M_c = 0$.

We start with a standard result, global energy balance for an isolated, i.e. not embedded, planet:

$$L_M = L_c + \Gamma - \dot{E}. \qquad (15)$$

The surface luminosity, L_M, includes the core luminosity L_c from e.g. planetesimal accretion or radioactive decay. The total heat generation Γ is the integral of ϵ over the atmosphere. The rate of change of atmospheric energy, $\dot{E}$, is a loss term.

For an object with no core luminosity (or no core) and no internal heat sources, the energy equation $L_M = -\dot{E}$ describes KH contraction in its simplest form. When internal heat sources dominate, $L_M = \Gamma$, e.g. for nuclear burning in a main sequence star.

A protoplanetary atmosphere embedded in a gas disk lacks a free surface. For objects without a free surface (or interior to a free surface), the full energy equation,

$$L_M = L_c + \Gamma - \dot{E} + e_M \dot{M} - P_M \left. \frac{\partial V_M}{\partial t} \right|_M \,, \qquad (16)$$

acquires surface terms as derived in Appendix A. The surface can be at any mass level M, where the instantaneous radius is R. Surface quantities are labeled by M subscripts (except for R). The energy accreted across the surface is given by the specific energy, $e_M = u_M - GM/R$, and the mass accretion rate of gas, $\dot{M}$. The work done by the surface is $P_M \partial V_M / \partial t$, with the partial derivative performed at fixed mass.

For static solutions, which are not the focus of this paper, the surface terms (and also $\dot{E}$) vanish. Static solutions are valid when imposed heat sources, i.e. L_c and Γ, exceed the atmospheric losses. Quantitatively, static solutions apply when the KH timescale,

$$\tau_{KH} \sim \frac{|E|}{L_M}, \qquad (17)$$

is shorter than the actual evolutionary timescale. Thus, τ_{KH}, which our models calculate, gives strong lower limits on the time to form giant planets by core accretion.

2.5. The Two-Layer Model

To simplify our evolutionary calculations, we develop a two-layer atmospheric model with a convective interior and a radiative exterior. The existence of this layered structure is well known from previous studies (e.g., R06) and can be readily understood. Before the protoplanetary atmosphere can cool, it has the entropy of the disk. As the atmosphere cools, the deep interior remains convective. Convective interiors are a common feature of low mass cool objects (brown dwarfs and planets) that results from the behavior of ∇_{rad} for realistic opacity laws. However, the entropy of the deep interior decreases as the atmosphere cools. A region of outwardly increasing entropy, i.e. a radiative layer, is required to connect the convective interior to the disk. A more complicated structure, with radiative windows in the convection zone, is possible as discussed in §6.2.

In convective regions, the adiabatic structure is independent of luminosity and can be calculated without local energy balance, Equation (10d). Thus, for fully convective objects, a cooling sequence can be established by connecting a series of adiabatic solutions using a global energy equation, $L_M = -\dot{E}$ or Equation (15). Such methods are commonly used for their computational efficiency and are sometime referred to as "following the adiabats," since the steady state solutions evolve in order of decreasing entropy (Marleau & Cumming 2013).

In the radiative zone, local energy balance, Equation (10d), does affect the atmospheric structure. We proceed by assuming that the majority of energy is lost from the convective interior, and thus the luminosity can be treated as constant in the outer radiative zone.

With this approximation for the radiative zone, we can construct an array of solutions to Equations (10a – c) in order of increasing atmospheric mass. We then use global energy balance, Equation (16), to "follow the mass" and place these solutions in a cooling sequence. The validity of neglecting luminosity generation in the radiative zone can be checked a posteriori, see §4.3.

To obtain a single atmosphere solution (indexed by i), we choose a planet mass M_i. At the outer boundary, at $R_H(M_i)$, the temperature and pressure are set to the disk values. To integrate Equations (10a–c), the luminosity is required to compute ∇_{rad}. The correct value of the luminosity is not known in advance, and is the eigenvalue of the problem. The boundary conditions can only be satisfied for the correct value of the luminosity eigenvalue, which we find by the shooting method. Specifically, we alter the luminosity until the integrated value of mass at the core, $m(R_c)$, matches the actual core mass, M_c.

To establish the time difference between neighboring solutions, we apply Equation (16) at the radiative-convective boundary (RCB) of the solutions. In principle, energy balance could be evaluated at any level. Our approximate treatment of the radiative zone makes the RCB the preferred location. The elapsed time Δt between states i and $i + 1$ is given by the finite difference

$$\Delta t = \frac{-\Delta E + \langle e \rangle \Delta M - \langle P \rangle \Delta V_{\langle M \rangle}}{\langle L \rangle} \,, \qquad (18)$$

using Equation (16) with $\Gamma = L_c = 0$. Brackets indicate an average of, and Δ indicates a difference between, the two states. All values are evaluated at the RCB. Due to the partial derivative in Equation (16), the volume difference $\Delta V_{<M>}$ is performed at fixed mass, here the average of the masses at the RCB.

3. ANALYTIC COOLING MODEL

This section develops the analytic version of our two-layer model. This analytic model is less accurate than our numerical model, primarily because it neglects self-gravity. We show (in §4) that self-gravity becomes important at rather low atmospheric masses, $M_{\rm atm} \gtrsim 0.1 M_c$. Nevertheless, the analytic model is useful for understanding atmospheric evolution and interpreting the numerical results.

The analytic model also assumes that the upper radiative layer is thick enough that $P_{\rm RCB} \gg P_{\rm d}$. This approximation ignores the earliest stages of cooling, which are rapid enough to be negligible. Finally, the analytic model ignores the surface terms in Equation (16), which we show to be a modest correction in §4.3.

3.1. *Two Layer Structure*

In order to apply the two-layer cooling model analytically, we require expressions for the atmospheric structure. Conditions at the RCB are crucial as they set the interior adiabat and the radiative losses from the interior. (Recall that luminosity generation in the radiative zone is neglected.) We express the temperature and pressure of the RCB, at the radius $R_{\rm RCB}$, as

$$T_{\rm RCB} = \chi T_{\rm d} \tag{19a}$$
$$P_{\rm RCB} = \theta P_{\rm d} e^{R_{\rm B}/R_{\rm RCB}}. \tag{19b}$$

The leading constants would be unity, $\chi = \theta = 1$, if the radiative zone were replaced by an isothermal layer. In practice, deviations from unity are modest. Standard radiative structure calculations (see Appendix B.2 for details) give

$$\chi \simeq \left(1 - \frac{\nabla_{\rm ad}}{\nabla_\infty}\right)^{-\frac{1}{4-\beta}} \simeq 1.53, \tag{20}$$

for $P_{\rm RCB} \gg P_{\rm d}$, our regime of interest, and with the radiative temperature gradient at depth, $\nabla_\infty = 1/2$, for our dust opacity. The radiative zones are thus nearly isothermal, as found by R06. A numerical integration gives $\theta \simeq 0.556$ for our parameters.

Given the conditions at the RCB, the density and temperature profiles along the interior adiabat,

$$\rho = \rho_{\rm RCB} \left[1 + \frac{R'_{\rm B}}{r} - \frac{R'_{\rm B}}{R_{\rm RCB}}\right]^{1/(\gamma-1)} \tag{21a}$$

$$T = T_{\rm RCB} \left[1 + \frac{R'_{\rm B}}{r} - \frac{R'_{\rm B}}{R_{\rm RCB}}\right], \tag{21b}$$

follow from hydrostatic balance. We introduce an effective Bondi radius

$$R'_{\rm B} \equiv \frac{GM_c}{C_P T_{\rm RCB}} = \frac{\nabla_{\rm ad}}{\chi} R_{\rm B} \tag{22}$$

to simplify expressions, with $C_P = \mathcal{R}/\nabla_{\rm ad}$ the specific heat capacity at constant pressure.

Deep in the adiabatic interior, where $r \ll R_{\rm RCB} \ll R'_{\rm B}$, the profiles follow simple power laws,

$$\rho \simeq \rho_{\rm RCB} \left[\frac{R'_{\rm B}}{r}\right]^{1/(\gamma-1)} \propto r^{-5/2} \tag{23a}$$

$$T \simeq T_{\rm RCB} \frac{R'_{\rm B}}{r} = \frac{GM_c}{C_P r}. \tag{23b}$$

While the radial density profile depends on the adiabatic index, the r^{-1} temperature scaling is universal. In self-gravitating models, the temperature gradient,

$$\frac{dT}{dr} = -\frac{Gm(r)}{C_P r^2}, \tag{24}$$

gives a profile that is flatter than $T \propto r^{-1}$.

Returning to our non-self-gravitating model, the total specific energy at depth,

$$e = e_g + u = -\nabla_{\rm ad} \frac{GM_c}{r}, \tag{25}$$

is simply proportional to the gravitational potential, $e_g = -GM_c/r$.

3.2. *Mass, Energy and Luminosity*

The most relevant quantities for global cooling are the integrated energy, luminosity, and atmospheric mass. In our non-self-gravitating limit, the mass of our nearly isothermal radiative zones is less than the convective interior, as shown in Appendix B.1.

The atmospheric mass is thus given by the integration of Equation (21a),

$$M_{\rm atm} = \frac{5\pi^2}{4} \rho_{\rm RCB} R'_{\rm B}{}^{5/2} \sqrt{R_{\rm RCB}}, \tag{26}$$

in the relevant limit $R_c \ll R_{\rm RCB} \ll R'_{\rm B}$ and for $\gamma = 7/5$. Mass is concentrated near the outer regions of the convective zone, a result that holds for $\gamma > 4/3$.

Using Equation (19b) to eliminate $R_{\rm RCB}$, the ratio of atmosphere to core mass becomes

$$\frac{M_{\rm atm}}{M_c} = \frac{P_{\rm RCB}}{\xi P_M}, \tag{27}$$

where we define a characteristic pressure and a logarithmic factor:

$$P_M \equiv \frac{4\nabla_{\rm ad}^{3/2}}{5\pi^2 \sqrt{\chi}} \frac{GM_c^2}{R'_{\rm B}{}^4} \tag{28a}$$

$$\xi \equiv \sqrt{\ln[P_{\rm RCB}/(\theta P_{\rm d})]}. \tag{28b}$$

The atmosphere mass increases as radiative losses lower the internal adiabat and increase $P_{\rm RCB}$. The crossover mass, $M_{\rm atm} = M_c$, is reached when

$$P_{\rm RCB} = \xi P_M, \tag{29}$$

i.e. near the characteristic pressure P_M. The critical value of the order unity factor ξ is found by eliminating $P_{\rm RCB}$ from Equations (28b) and (29). This logarithmic factor complicates our analytic description. Since it remains order unity, we simply hold it fixed in our scalings.

The total energy is concentrated towards the core if $|e|\rho r^3 \propto \rho r^2$ drops with increasing r. This condition requires $\gamma < 3/2$, which our choice of $\gamma = 7/5$ satisfies,

but $\gamma = 5/3$ (monatomic gas) would not. Integration of Equation (25) over the mass of the atmosphere thus gives

$$E = -4\pi \nabla_{\rm ad} G M_{\rm c} \int_{R_{\rm c}}^{R_{\rm RCB}} \rho r \, dr \qquad (30a)$$

$$\approx -4\pi P_{\rm RCB} R'_{\rm B}{}^{\frac{1}{\nabla_{\rm ad}}} \left(\frac{\gamma - 1}{3 - 2\gamma} \right) R_{\rm c}^{\frac{2\gamma - 3}{\gamma - 1}} \qquad (30b)$$

$$\approx -8\pi P_{\rm RCB} \frac{R'_{\rm B}{}^{7/2}}{\sqrt{R_{\rm c}}}, \qquad (30c)$$

with $\gamma < 3/2$ and $\gamma = 7/5$ in Equations (30b) and (30c), respectively.

The emergent luminosity from the RCB,

$$L_{\rm RCB} = \frac{64\pi G M_{\rm RCB} \sigma T_{\rm RCB}^4}{3\kappa P_{\rm RCB}} \nabla_{\rm ad} \approx L_{\rm d} \frac{P_{\rm d}}{P_{\rm RCB}}, \qquad (31)$$

follows from Equation (11) and marginal convective stability, $\nabla_{\rm rad} = \nabla_{\rm ad}$, where we define

$$L_{\rm d} \equiv \frac{64\pi G M_{\rm RCB} \sigma T_{\rm d}^4}{3\kappa(T_{\rm d}) P_{\rm d}} \nabla_{\rm ad} \chi^{4-\beta}. \qquad (32)$$

The scaling $L_{\rm RCB} \propto 1/P_{\rm RCB}$ shows that luminosity drops as the atmosphere cools and $P_{\rm RCB}$ deepens. This result relies on the pressure independence of dust opacities. For fully non-self-gravitating results, we replace $M_{\rm RCB}$, the mass up to the RCB, with the core mass, but the mass of the convective atmosphere can be included for a slightly higher order estimate.

3.3. Cooling Times & Core Masses

Our analytic cooling model uses $L = -\dot{E}$, neglecting the surface terms in Equation (16).[3] Applying Equations (30c) and (31), the time it takes to cool the atmosphere until the RCB reaches a given pressure depth, $P_{\rm RCB}$, is

$$t_{\rm cool} = -\int_{P_{\rm d}}^{P_{\rm RCB}} \frac{dE/dP_{\rm RCB}}{L_{\rm RCB}} dP_{\rm RCB} \qquad (33a)$$

$$\approx 4\pi \frac{P_{\rm RCB}^2}{P_{\rm d}} \frac{R'_{\rm B}{}^{7/2}}{L_{\rm d}\sqrt{R_{\rm c}}}. \qquad (33b)$$

The initial RCB depth is set to $P_{\rm d}$ as a formality. The cooling slows as it proceeds with $t_{\rm cool} \propto P_{\rm RCB}^2$.

We expect runaway growth to begin around the crossover mass, $M_{\rm atm} = M_{\rm c}$. Equations (33) and (29) give the time to crossover as

$$t_{\rm co} \approx 2 \times 10^8 \frac{F_T^{5/2} F_\kappa \left(\frac{\xi}{3.4} \right)^2}{m_{\rm c10}^{5/3} a_{10}^{15/14}} \ {\rm yr} \,. \qquad (34)$$

We estimate the critical core mass, $M_{\rm crit}$, by equating the crossover time with a typical protoplanetary disk lifetime,

$$t_{\rm d} = 3 \times 10^6 \ {\rm yr} \,. \qquad (35)$$

Setting $t_{\rm co} = t_{\rm d}$ gives

$$M_{\rm crit} \approx 100 \frac{F_T^{3/2} F_\kappa^{3/5} \left(\frac{\xi}{2.6} \right)^{6/5}}{a_{10}^{9/14}} \ M_\oplus. \qquad (36)$$

[3] Appendix B.4 shows that these terms are negligible for a non-self-gravitating model.

Both $t_{\rm co}$ and $M_{\rm crit}$ are too large to be interesting, or to be correct based on previous results and the numerical results in this paper. The main reason for this discrepancy is the neglect of self-gravity. Section 4 explores in detail the effects of self-gravity on atmospheric structure, luminosity and evolution. One might expect self-gravity to be only a modest correction for $M_{\rm atm} \le M_{\rm c}$. This seemingly reasonable expectation can be misleading, an interesting result in itself.

Aside from this insight, the analytic model is useful because, despite the amplitude error, it explains the basic scaling of numerical cooling models. As is well known (Hubickyj et al. 2005), a lower opacity, here scaling with F_κ, allows faster cooling and gives a lower critical core mass. The cooling timescale and critical core mass depend only weakly on the disk pressure, via the logarithmic factor ξ. The almost exponential rise in radiative zone pressure with depth, see Equation (19b), explains why disk pressure has only a weak effect on cooling at the RCB.

Lower disk temperatures decrease both $t_{\rm co}$ and $M_{\rm crit}$. The decline in both quantities with semimajor axis is completely explained by the temperature profile (ignoring the logarithmic factor ξ). The temperature dependence is a competition between two main effects. The Bondi radius, which quantifies the strength of gravity, decreases for lower temperatures. On the other hand, the luminosity, $\propto T^{4-\beta}$, is lower at colder temperatures, which slows cooling and opposes the overall effect. With $t_{\rm co} \propto F_T^{\beta+1/2}$, the slope of the dust opacity, β, is an important factor in regulating the resulting growth time.

To facilitate comparison with our numerical results, we rescale the analytic results as a rough correction for the neglect of self gravity. The goal of the rescaling is not to get a perfect agreement, but to aid in the interpretation of general trends. To rescale, we simply assume that runaway occurs at a modified crossover mass, $M_{\rm atm} = f M_{\rm c}$. From Equations (27) and (29), this change amounts to replacing $\xi \to f\xi$. We require $f < 1$ to give the faster growth seen in numerical models. We choose $f = 0.13$, which normalizes the analytic and numerical models at 10 AU, for standard parameters. The revised scalings are

$$t_{\rm run} \approx 3 \times 10^6 \frac{F_T^{5/2} F_\kappa \left(\frac{\xi}{3.4} \right)^2}{m_{\rm c10}^{5/3} a_{10}^{15/14}} \ {\rm yr} \qquad (37a)$$

$$M_{\rm crit} \approx 8 \frac{F_T^{3/2} F_\kappa^{3/5} \left(\frac{\xi}{2.6} \right)^{6/5}}{a_{10}^{9/14}} \ M_\oplus \,, \qquad (37b)$$

now using $t_{\rm run}$ instead of $t_{\rm co}$ for the runaway growth timescale, which is no longer tied to the crossover mass. The numerical models are more accurate and self-consistent because they measure runaway growth directly, instead of relying on any assumed $M_{\rm atm}/M_{\rm c}$ threshold. When plotting the analytic scalings, we include the variations in ξ from Equation (28b).

4. QUASI-STATIC KELVIN-HELMHOLTZ CONTRACTION

We examine the structure and evolution of our model atmospheres, calculated as described in §2. For com-
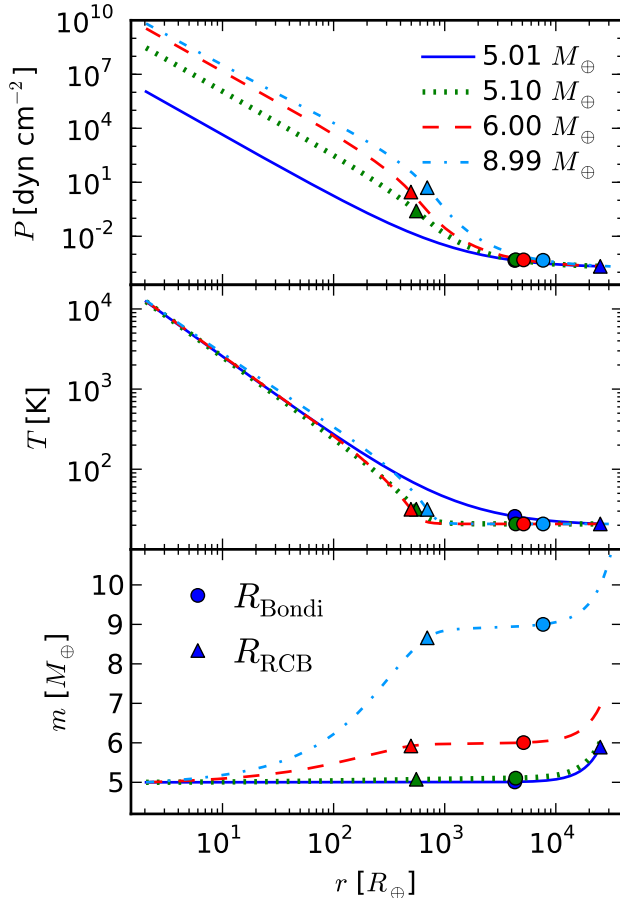
FIG. 1.— Radial profiles of atmospheric pressure, temperature and enclosed mass (core included) for a $5M_\oplus$ core at 60 AU. Solid, dotted, dashed and dot-dashed lines correspond to solutions with total mass (core and atmosphere) of $5.01M_\oplus$, $5.10M_\oplus$, $6.00M_\oplus$ and $8.99M_\oplus$, respectively (see text for significance of these masses). Circles and triangles mark the locations of the Bondi radii and of the radiative-convective boundaries, respectively. The radial profiles extend from the core to the Hill radius.

parison, we also show results of the non-self-gravitating analytic model of §3. Radial structure is presented in §4.1, time evolution is described in §4.2, and the validity of our two-layer cooling model is examined in §4.3.

4.1. Atmospheric Structure

Figure 1 shows radial profiles at different stages of atmospheric growth around a $5M_\oplus$ core at 60 AU. Quoted mass values include the core plus atmosphere within the smaller of R_B or R_H, which for these cases is R_B. The $8.99~M_\oplus$ solution is the mass that satisfies our runaway growth criteria (described in §4.2).

The lowest mass atmosphere – which we take as our initial state – is fully convective and shares the disk's entropy. In Figure 1 this state is the $5.01~M_\oplus$ solution with no radiative zone.

Cooling and contraction allow the atmosphere to accrete more gas. In the convective zones, higher mass solutions have lower entropy and higher pressures. A radiative zone emerges to connect the lower entropy interior to the higher entropy disk. Figure 1 shows that
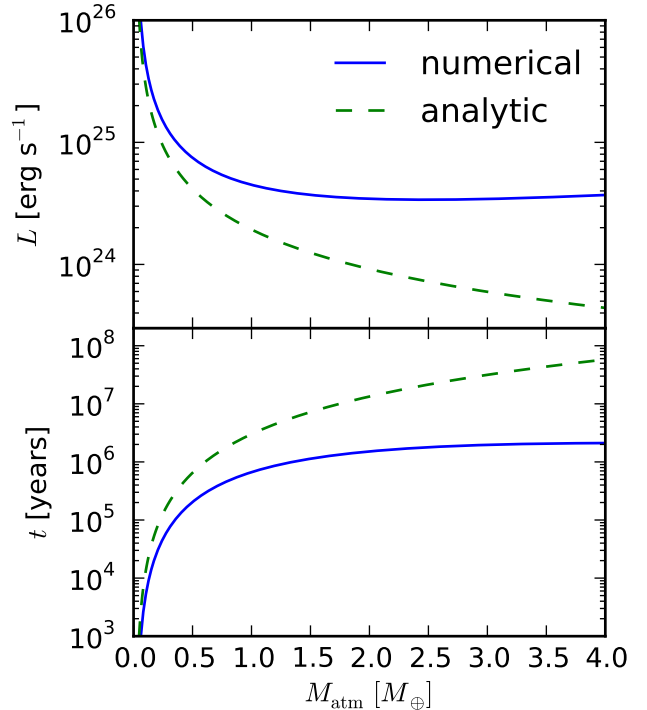

FIG. 2.— Evolution of the luminosity and elapsed time during atmospheric growth around a $5M_\oplus$ core at 60 AU. The luminosity is initially high, then decreases as the atmosphere grows in mass and the radiative zone becomes optically thicker. Due to the neglect of self-gravity, the analytic model (*dashed curve*) gives luminosities that are too low and evolution times that are too long.

this radiative zone is already fairly deep in the $5.10~M_\oplus$ solution.

The atmospheric structure is well approximated by our non-self-gravitating, analytic solutions. Deep in convective zones, Equation (23) gives $T \propto r^{-1}$ and $P \propto r^{-1/\nabla_{\rm ad}}$. This behavior is seen in the low mass solutions in Figure 1. As explained by Equation (24), the high mass solutions show a slightly flatter profile in T and also in $P \propto T^{1/\nabla_{\rm ad}}$. In agreement with Equation (19), the radiative zones remain nearly isothermal, even for the higher masses. Consequently, the pressure increases nearly exponentially with depth.

4.2. Time Evolution

The cooling model of §2.5 is used to connect solutions with different atmospheric masses into an evolutionary sequence. Figure 2 shows the luminosity evolution and the elapsed time as a function of atmospheric mass for the same parameters as in Figure 1.

During the early stages of atmospheric growth, the luminosity drops sharply. This behavior is seen in both the full numerical solutions and the analytic model. With increasing atmospheric mass, the pressure depth of the RCB increases, along with the optical depth ($\propto \kappa P_{\rm RCB}$). Consequently, the radiative luminosity decreases. This behavior is described in Equations (27) and (31).

At later stages of evolution, the numerical model in Figure 2 shows a flat luminosity with increasing mass and also time (not shown). By contrast, the non-self-

gravitating analytic model gives a luminosity that continues to drop as the atmosphere becomes more massive. To understand this difference, consider the scaling of Equation (31), $L_{\mathrm{RCB}} \propto M_{\mathrm{RCB}} T_{\mathrm{RCB}}^4/(\kappa_{\mathrm{RCB}} P_{\mathrm{RCB}})$, which holds in both cases. Accounting for the higher enclosed mass in the self-gravitating model gives a somewhat higher luminosity, as desired. However, the main effect is that Equation (27) – which describes a nearly linear relation between atmospheric mass and RCB pressure – breaks down for self-gravitating solutions. This behavior can be seen in the top panel of Figure 1 where the P_{RCB} increases significantly from 5.10 to 6.0 $M_\oplus$, but only increases relatively modestly with further growth to 8.99 $M_\oplus$. In the higher mass solutions, the relatively low P_{RCB} values (and thus the relatively high luminosities) require an outward shift in R_{RCB}, as shown in Figure 1.

The accelerated growth in the numerical model, as shown in the bottom panel of Figure 2, is also a direct result of the higher cooling luminosities in the self-gravitating models. We see that self-gravity strongly affects atmospheric evolution, even well before the crossover mass, when $M_{\mathrm{atm}} = M_{\mathrm{c}}$.

In Figure 3, our standard dust opacity, Equation (5), is reduced by factors of 10 and 100. Lower opacities result in higher luminosities and faster evolution. Our model thus confirms a well-established result (Hubickyj et al. 2005). While clearly an important effect, atmospheric dust opacities are difficult to robustly predict. Ablation of infalling solids is a dust source. Sinks include the sequestration of solids in the core and dust settling through the radiative zone. Grain growth both reduces dust opacities per unit mass and favors settling. Our scenario of negligible ongoing particle accretion tends to favor low dust opacities. To be conservative, however, our reference case considers full Solar abundances. The effect of opacity reduction on the critical core mass is described in §5.

Figure 4 plots the evolution of the atmospheric growth timescale, $M_{\mathrm{atm}}/\dot{M}$, around a $5M_\oplus$ core at several locations in our reference disk model. This instantaneous growth time shows clearly that the atmosphere spends the bulk of its time growing though intermediate atmospheric masses, $\sim 1 - 3\ M_\oplus$ in this case. Growth times are short both early – when the radiative zone is transparent – and late – when self-gravity accelerates growth.

The fact that growth times have a well defined maximum is a characteristic of accelerating growth. Unlike our analytic model, which must assume that runaway growth begins near the crossover mass, our numerical model allows us to measure when runaway accretion starts. Runaway growth does not begin at a universal value of $M_{\mathrm{atm}}/M_{\mathrm{c}}$. Further from the star, runaway growth begins at smaller $M_{\mathrm{atm}}/M_{\mathrm{c}}$, as Figure 4 shows. Figure 6 (described in the next section) shows how the onset of runaway growth depends on core mass.

We quantify the runaway growth timescale, t_{run}, as the time when $M_{\mathrm{atm}}/\dot{M}$ drops to 10% of its maximum value. The choice of 10% is arbitrary; the precise threshold chosen is relatively unimportant because growth continues to accelerate.

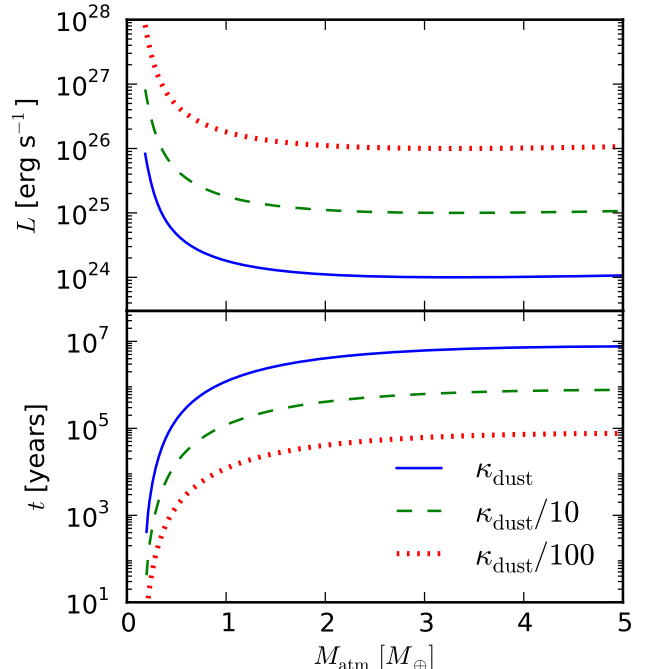### 4.3. Validity of the Two-Layer Cooling Model

FIG. 3.— The effect of dust abundance on atmospheric evolution. Reducing dust opacities by factors of 10 and 100 from standard Solar abundances gives higher luminosities and faster atmospheric growth. Plotted quantities are similar to Figure 2, but for a $5M_\oplus$ core at 10 AU.
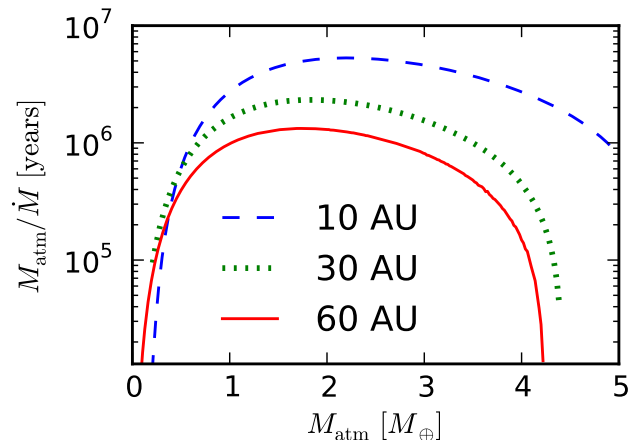

FIG. 4.— Evolution of the atmospheric growth timescale with mass around a $5M_\oplus$ solid core located at 10, 30 or 60 AU, for standard Solar opacities. Growth is slowest for $M_{\mathrm{atm}} \sim 1 - 3M_\oplus$, i.e. before the crossover mass at $M_{\mathrm{atm}} = M_{\mathrm{c}}$.

We examine the validity of our cooling model by comparing our model luminosity to the neglected luminosity, L_{negl}, that a more detailed model would generate in the radiative zone. We compute L_{negl} from the entropy difference between successive radiative zone solutions. We then integrate the energy equation, $\partial L/\partial m = -T\partial S/\partial t$,
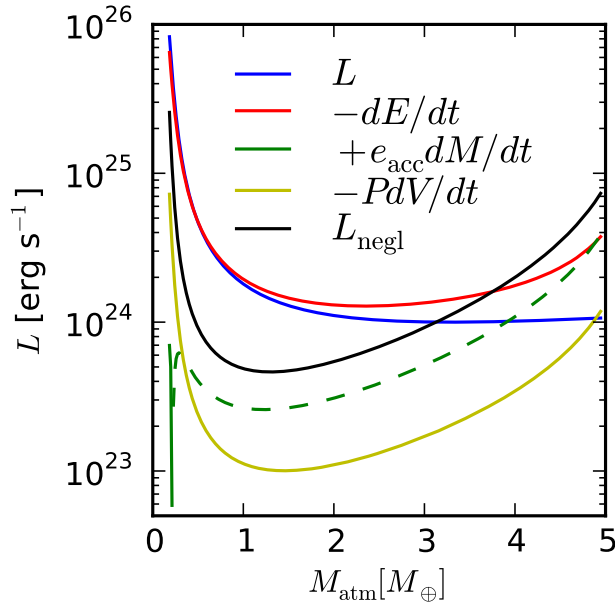
FIG. 5.— Individual terms in the atmospheric cooling model of Equation (16), for a $5M_\oplus$ core at 10 AU. The dashed curve for accretion energy indicates a negative contribution. All quantities are evaluated at the RCB, except for $L_{\rm negl}$, the extra luminosity that would have been generated in the radiative zone, but is neglected in our model. The neglected luminosity is a small correction to the model luminosity L for $M_{\rm atm} \lesssim 3M_\oplus$. Since these low masses dominate growth times, our model is roughly accurate.

over the average depth of the radiative zone.[4]

Figure 5 shows that the neglected luminosity is indeed negligible during the early stages of evolution. However, $L_{\rm negl}$ exceeds the model luminosity, L, at high masses, $M_{\rm atm} > 3M_\oplus$ in this case. Our cooling model is thus inaccurate at higher masses. However, the model remains reasonably accurate up to the beginning stages of runaway growth, which is sufficient for our purposes of widely exploring parameter space and exploring trends.

The individual terms in the global cooling model of Equation (16), evaluated at the RCB, are also plotted in Figure 5. At low masses, the change in energy, $-\dot{E}$, makes the dominant contribution to luminosity. As the mass increases, the surface terms become more significant, led by the accretion energy. However, the surface terms are everywhere smaller than $L_{\rm negl}$. Thus wherever our model is accurate – including the crucial early phases of growth – surface terms are a minor correction. The neglect of surface terms in the analytic model is thus not a serious omission.

5. RESULTS FOR GIANT PLANET FORMATION

We now use our structure and evolution models to calculate the necessary conditions for gas giant formation by core accretion. Adopting a median disk lifetime of 3 Myr, we examine the conditions for a fixed mass core to undergo runaway gas accretion within the lifetime of the gas disk. Our results for atmosphere growth times

[4] While useful as a diagnostic, the neglected luminosity cannot reliably correct the global cooling model because the effects of $L_{\rm negl}$ on the structure of the radiative zone are still ignored.
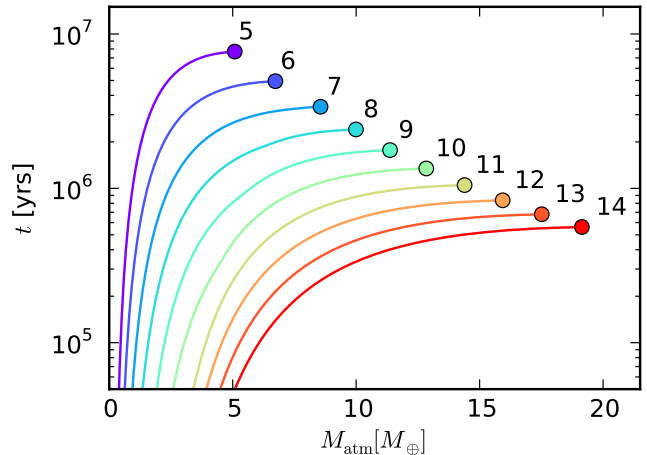

FIG. 6.— Time to grow an atmosphere of mass $M_{\rm atm}$ for cores with fixed masses between $5M_\oplus$ and $14M_\oplus$ (as labeled) at 10 AU in our fiducial disk. Circles mark the runaway growth time, $t_{\rm run}$, which occurs at roughly the crossover mass, $M_{\rm atm} = M_{\rm c}$. Both the time to reach a fixed atmosphere mass and the runaway growth time are shorter for larger cores. For larger $M_{\rm c}$, runaway growth commences at higher $M_{\rm atm}/M_{\rm c}$ values.

– for a range of core masses and disk conditions – are presented in §5.1. Section 5.2 gives our results for critical core masses, the minimum masses needed to accrete a massive atmosphere within the disk lifetime.

Our models focus on giant planet formation between 5 and 100 AU, as the outer disk is of particular interest for direct imaging searches. The growth of atmospheres close to the star is also important, but spherical accretion models (including ours) are less applicable here. In the inner disk, critical core masses increase, yet lower mass planets start to open gaps and outgrow the disk scale height, see Equation (9). These concerns prevent us from applying our model to the inner disk.

5.1. Runaway Growth Timescale

The time to undergo atmospheric runaway growth, $t_{\rm run}$, sets a minimum timescale for the formation of giant planets. Due to the accelerating nature of runaway growth, the precise threshold chosen for $t_{\rm run}$ (explained in §4.2) is of minor significance.

5.1.1. Effects of Core Mass

Figure 6 shows the growth of atmospheric mass with time for several core masses at 10 AU in our fiducial disk. Atmospheres grow faster around more massive cores due to stronger gravitational binding. The endpoint of each curve marks $t_{\rm run}$. Runaway growth occurs near the crossover mass, when $M_{\rm atm} \sim M_{\rm c}$, in agreement with previous studies. Lower core masses undergo runaway accretion at fractionally smaller atmosphere masses.

Figure 7 shows how $t_{\rm run}$ varies with core mass, also at 10 AU. The numerical results are plotted against our non-self-gravitating analytic model, described in §3. The analytic model reproduces the general decline in $t_{\rm run}$ with core mass. The numerical model, which includes self-gravity, has a somewhat steeper mass dependence. A modest correction due to self-gravity is unsurprising, and consistent with the above-mentioned trend in $M_{\rm atm}/M_{\rm c}$
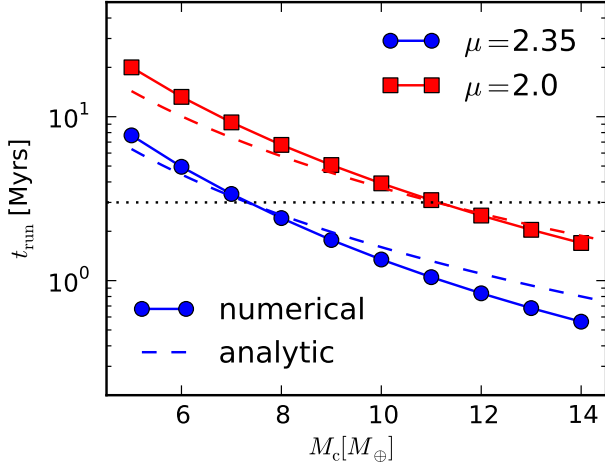
FIG. 7.— Runaway growth time, $t_{\rm run}$, vs. core mass at 10 AU, for two values of the mean molecular weight. Our numerical model (*solid curves*) is compared to our non-self-gravitating analytic model (*dashed curves*, from Equation 37a). A typical protoplanetary disk life time of 3 Myr is plotted for comparison. The runaway growth time is larger for a lower mean molecular weight.

ratios. Moreover, in the analytic theory, crucial quantities like $M_{\rm atm}$ and L (both roughly $\propto M_c^3$ near crossover) have non-linear dependence on core mass, offering plenty of opportunity for self-gravitational corrections.

The effect of mean molecular weight is also shown in Figure 7. A lower μ gives longer growth times, because more cooling is required to compress the atmosphere. This effect is explained by the increase in the atmospheric scale height $\propto 1/\mu$ while the Bondi radius decreases, $R_{\rm B} \propto \mu$. For $\mu = 2.0$, which represents the idealized case of an H_2 atmosphere completely devoid of Helium, $t_{\rm run}$ increases by factors of $\sim 2 - 3$. Thus fairly drastic changes in atmospheric composition are required for μ to significantly affect core accretion timescales.

5.1.2. *Effects of Disk Temperature and Pressure*

Figure 8 shows how the runaway accretion time varies with disk temperature, $T_{\rm d}$, or pressure, $P_{\rm d}$, holding the other quantity fixed. The analytic model roughly reproduces the temperature and pressure scalings, again with some discrepancies due mainly to the neglect of self-gravity. Temperature variations are much more significant than pressure variations (note the difference in logarithmic and linear axes). Since midplane disk conditions depend only on temperature and pressure in our model,[5] the dominant effect of disk location is temperature.

The decline in growth times with lower temperatures arises from a balance of competing effects. The cooling luminosity is inherently smaller at lower temperatures. Overpowering this effect, the larger Bondi radius and lower dust opacity act to accelerate growth at lower temperatures.

Growth times depend only weakly on, but do fall slightly with, pressure. This result may be surprising,

---

[5] See Equation (1). When gap opening is considered in models of later growth stages, the orbital frequency and effective viscosity become relevant as well.

given that the disk is the source of atmospheric mass and the atmosphere must match onto the disk's density and pressure. The nearly exponential increase in pressure with depth through the radiative zone explains this effect. Cooling is largely regulated at the RCB, and a modest change in RCB depth compensates for large variations in disk pressure.

Section 3 shows how these temperature and pressure effects arise in our analytic model.

5.2. *Critical Core Mass*

The critical core mass declines with distance from the star, as shown in Figure 9 for our standard disk model. The main reason for the decline, as explained above, is that atmospheres grow faster at lower temperatures. The lower densities and pressures in the outer disk have a much smaller effect. Since the vast majority of disk models have a disk temperature that declines with a, our qualitative result is robust. We also show that higher μ values give lower values of $M_{\rm crit}$.

The average power-law decline from 1 to 100 AU (not plotted) is $M_{\rm crit} \propto a^{-0.3}$, for both choices of μ. While not a drastic decline, the ability of distant low mass cores to accrete gas efficiently is significant for the interpretation of direct imaging surveys. However, our model offers no guarantee of copious giant planets at large distances. Many histories of solid accretion are possible, and solid cores may grow too slowly to allow the rapid gas accretion that we model.

Our non-self-gravitating analytic model (dashed curves in Figure 9) over-predicts the steepness of the decline in $M_{\rm crit}$ with a. This discrepancy is not surprising, as we have shown that self-gravity strongly affects evolution, even before runaway growth begins and the crossover mass is reached.

Figure 10 shows that reducing the opacity by an order of magnitude significantly reduces $M_{\rm crit}$. Furthermore, this opacity effect is stronger at larger distances. The opacity reduction by a factor of 10 lowers $M_{\rm crit}$ at 5 AU by a factor of $\sim$2.5 and at 100 AU by a factor of $\sim$3.5. Atmospheric opacity is a dominant uncertainty in core accretion modelling. However, unless atmospheric opacity varies significantly with disk radius, the general decline in $M_{\rm crit}$ with increasing a should hold. For our scenario of negligible ongoing planetesimal accretion, it is tempting to think that dust could settle out of the radiative zone, lowering the opacity (Podolak 2003). Nonetheless, since opacity near the RCB is a crucial factor, we speculate that convective overshoot may prevent very low opacities.

6. NEGLECTED EFFECTS

6.1. *Hydrodynamic Effects*

The neglect of hydrodynamical effects in our model is best discussed in terms of the thermal mass, $M_{\rm th}$, and the length scales introduced in §2.2. In the low mass regime, $M_{\rm p} < M_{\rm th}/\sqrt{3}$, where $R_{\rm B} < R_{\rm H}$, we assume that hydrostatic balance holds out to the outer boundary at $R_{\rm H}$. In this low mass regime, Ormel (2013) calculated the flow patterns driven by stellar tides and disk headwinds. On scales $\gtrsim R_{\rm B}$ the flows no longer circulate the planet: they belong to the disk. Nevertheless, the density structure outside $R_{\rm B}$ remains spherically symmetric and
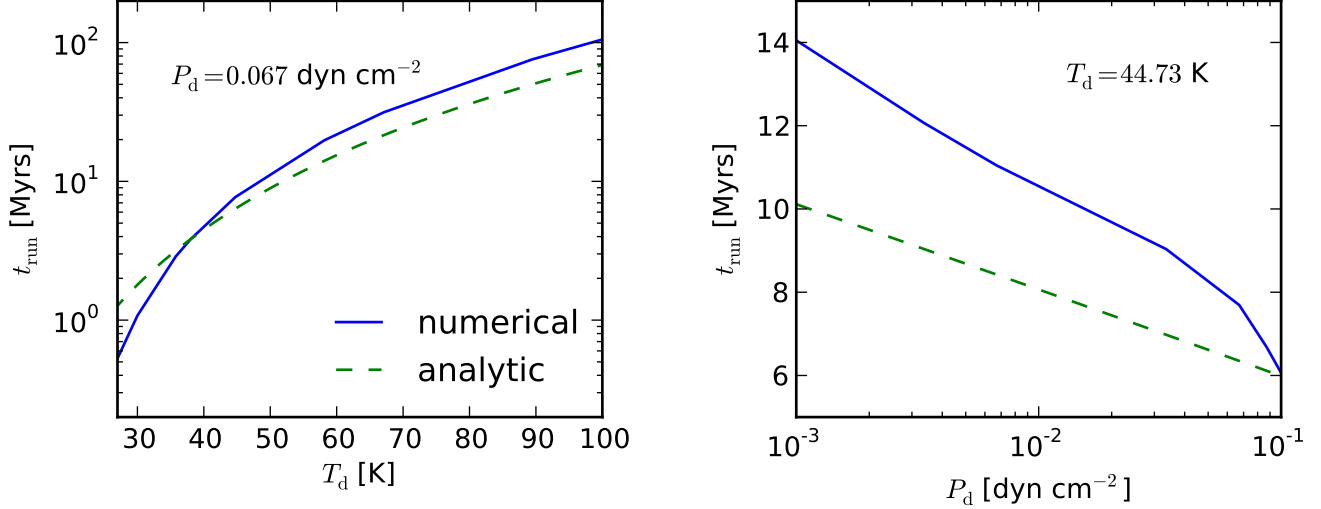
FIG. 8.— Runaway growth time as a function of disk temperature (*left*) and pressure (*right*) around a $M_c = 5M_\oplus$ core. The disk pressure or temperature (*left* or *right*, respectively) are fixed at values for 10 AU in our disk model. The analytic scalings given by Equation (37a) are plotted for comparison, as described in the text. Gas accretion slows down significantly at higher temperatures, but only speeds up modestly as the disk pressure or density increase.
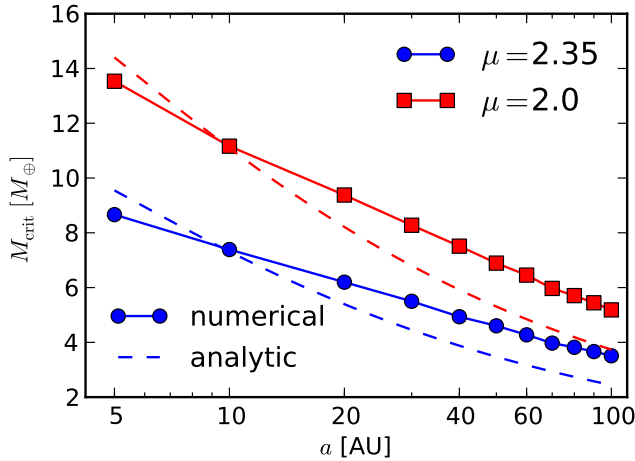

FIG. 9.— The critical core mass as a function of semimajor axis, for a disk lifetime of 3 Myrs and two values of the mean molecular weight ($\mu = 2.35$ is for Solar abundances). The decline in M_{crit} with distance is a robust result for standard disk models. The analytic model, which neglects self-gravity, over-predicts the steepness of the decline.
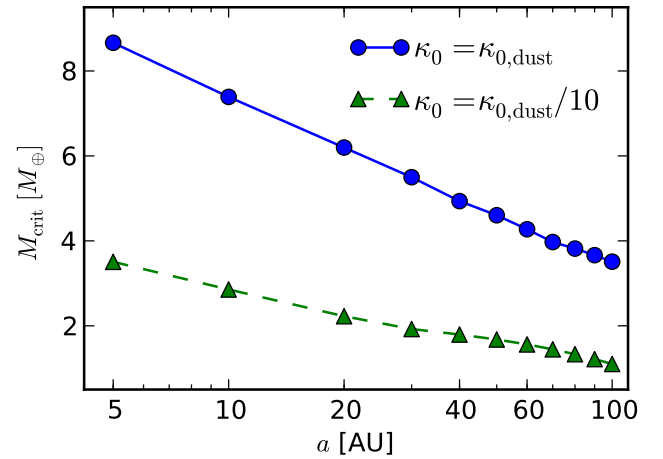
FIG. 10.— Critical core masses vs. distance for standard and reduced (by a factor of ten) dust opacities. Lower opacities give significantly lower M_{crit} values. Atmospheric opacity remains a large uncertainty in core accretion models.

hydrostatic. Even if these flows do not destroy hydrostatic balance, they could affect the planet's cooling. We expect such effects to be weak, as heat losses at greater depths dominate planetary cooling, but more study is needed.

At higher masses, non-hydrostatic effects become more severe. At $M_p \gtrsim M_{th}$ planets can open significant gaps (Zhu et al. 2013). At yet higher masses accretion instabilities could occur (Ayliffe & Bate 2012). However, in this high mass regime, the spherically symmetric approximation has already broken down.

Thus by restricting our attention to low masses, neglected hydrodynamic effects should be minor. Moreover, since $M_{th} \propto a^{6/7}$ increases with disk radius, spherical hydrostatic models like ours have a greater range of

applicability in the outer regions of disks.

6.2. *Realistic Opacities*

Treating dust (and total) opacities as a power law in temperature is a simplification. Opacities drop by order unity when ice grains sublimate for $T \gtrsim 150$ K and they drop by orders of magnitude when silicate grains evaporate above $T \gtrsim 1500$ K (Semenov et al. 2003; Ferguson et al. 2005). Grain growth and composition also affect opacities. Piso et al. (in prep.) explores more realistic opacity laws.

For this work, we justify a simplified dust opacity by the cool temperatures of both the outer disk and our nearly isothermal radiative zones (see §4.1). While convective interiors get significantly hotter than 1500 K, opacity does not affect the structure of adiabatic convecting regions. A possible caveat is the existence of ra-

diative zones sandwiched inside the convection interior. Such "radiative windows" arise if the opacity drop from ice and metal grain sublimation occurs at sufficiently low pressures. Our two-layer model ignores this possibility, but radiative windows are known to exist in hot Jupiter models (Burrows et al. 1997; Arras & Bildsten 2006) and have been seen in some core accretion models (Lissauer, personal communication). The role of radiative windows in core accretion models remains to be explored in detail.

6.3. *Equation of State*

Our model uses an ideal gas law and a polytropic EOS, given by Equation (13). However, non-ideal effects can affect atmospheric structure and evolution. In the lower atmosphere, H_2 can partially dissociate at high temperatures. In the upper atmosphere, H_2 rotational levels can become depopulated at lower temeratures. Piso et al. (in prep) uses the Saumon et al. (1995) EOS, with extensions to lower pressures and temperatures as needed, to explore these effects.

6.4. *Core growth*

Our model purposefully neglects the accretion of solids to study the fastest rates of gas accretion. Our M_{crit} values thus differ from the M_{crit} values in static models, such as R06. For similar parameters, we generally obtain lower M_{crit} values than R06 because our atmospheres are not heated by ongoing planetesimal accretion. Piso et al. (in prep) presents a quantitative comparison.

At low planetesimal accretion rates, $\dot{M}_c$, a static model could formally give lower M_{crit} values than our evolutionary calculations. R06 shows that $M_{crit} \propto \dot{M}_c^{3/5}$ in static models. The underlying assumption of static models, a negligibly short KH contraction time, fails whenever static models give a lower M_{crit}. Thus our results give a firm lower limit on M_{crit} which complement the results of static models with planetesimal accretion.

7. SUMMARY

We study the formation of giant planets by the core accretion mechanism. Our models start with a solid core that is embedded in a gas disk and no longer accreting solids. We determine – as a function of disk location, core mass, and the atmosphere's mean molecular weight and opacity – whether runaway atmospheric growth can occur within a typical disk lifetime of 3 Myr. By neglecting the accretion luminosity of planetesimals and smaller solids, we obtain the fastest allowed rate of gas accretion.

We address core accretion in the outer disk, as it is relevant to direct imaging surveys. Our model approximations, including spherical accretion and low mass radiative exteriors with opacities dominated by dust, are tuned to conditions in the outer disk. Our main findings are as follows:

1. The minimum or critical core mass, M_{crit}, for giant planet formation declines with stellocentric distance in standard protoplanetary disk models. For our reference case, the critical mass is $\sim 8.5 M_\oplus$ at $a = 5$ AU, decreasing to $\sim 3.5 M_\oplus$ at $a = 100$ AU. This decline roughly follows $M_{crit} \propto a^{-0.3}$.

2. The drop in disk temperature with radial distance explains the decrease in critical core masses. The lower pressures and densities in the outer disk only weakly suppress atmospheric growth.

3. Reducing dust opacities by a factor of 10 reduces critical core masses by a factor of ~ 3. This reduction is somewhat stronger (weaker) at larger (smaller) separations from the star.

4. A larger mean molecular weight reduces critical core masses, in agreement with Hori & Ikoma (2011). If enrichment in heavy elements correlates with increased dust opacity, then the stronger opacity effect will dominate, increasing M_{crit}.

5. Runaway growth begins roughly at the crossover mass, when atmosphere and core masses are equal, $M_{atm} \sim M_c$, in agreement with previous work (Pollack et al. 1996). Further from the star, runaway growth begins at smaller $M_{atm} \sim M_c$ ratios. For larger core masses, runaway growth begins at larger values of $M_{atm} \sim M_c$.

6. Self-gravity affects atmospheric evolution before crossover. Significant self-gravitational corrections appear when the atmosphere is only $\sim 10\%$ as massive as the core.

Rapid gas accretion onto low mass cores could explain the origin of distant directly imaged giant planets (Marois et al. 2008; Lagrange et al. 2010). However, our model does not address the details of how solid cores grow, and many possibilities exist. For a giant planet to form with a core near the minimum mass, the core's growth must first be rapid and then slow significantly, as in phases I and II, respectively, of Pollack et al. (1996).

Initial core growth must be fast, compared to the disk lifetime, to get a sufficiently massive core. Subsequent slowing of core growth is required to allow the atmosphere to cool and contract. To be more quantitative, the minimum cooling luminosity in Figure 2, $L \approx 3.5 \times 10^{24}$ ergs^{-1}, could be cancelled by low levels of heating from solid accretion. Specifically, a core mass doubling timescale of ~ 400 Myr, or faster, would provide enough heating to stall atmospheric cooling and growth.

Thus for giant planets to form around cores near M_{crit}, core growth must stall quite severely. The accretion and scattering of local planetesimals, combined with the inward aerodynamic drift of smaller solids past the core, offers a plausible means to sufficiently isolate the core.

On the other hand, non-negligible accretion of solids onto cores could continue for the lifetime of the gas disk. In these cases, relatively high mass cores would remain as ice giants, akin to Uranus and Neptune. Ongoing direct imaging surveys and their successors (Hinz et al. 2012; Macintosh et al. 2012) will help discriminate among the various planet formation pathways in the outskirts of protoplanetary disks.

REFERENCES

Alibert, Y., Mordasini, C., Benz, W., & Winisdoerffer, C. 2005, A&A, 434, 343
Andrews, S. M., Wilner, D. J., Hughes, A. M., Qi, C., & Dullemond, C. P. 2010, ApJ, 723, 1241
Arras, P. & Bildsten, L. 2006, ApJ, 650, 394
Ayliffe, B. A. & Bate, M. R. 2012, MNRAS, 427, 2597
Bell, K. R. & Lin, D. N. C. 1994, ApJ, 427, 987
Bodenheimer, P. & Pollack, J. B. 1986, Icarus, 67, 391
Boss, A. P. 1997, Science, 276, 1836
Bromley, B. C. & Kenyon, S. J. 2011, ApJ, 731, 101
Burrows, A., Marley, M., Hubbard, W. B., Lunine, J. I., Guillot, T., Saumon, D., Freedman, R., Sudarsky, D., & Sharp, C. 1997, ApJ, 491, 856
Cameron, A. G. W. 1978, Moon and Planets, 18, 5
Chiang, E. & Youdin, A. N. 2010, Annual Review of Earth and Planetary Sciences, 38, 493
D'Angelo, G., Durisen, R. H., & Lissauer, J. J. Giant Planet Formation, ed. S. Piper, 319–346
Dones, L. & Tremaine, S. 1993, Icarus, 103, 67
Ferguson, J. W., Alexander, D. R., Allard, F., Barman, T., Bodnarik, J. G., Hauschildt, P. H., Heffner-Wong, A., & Tamanai, A. 2005, ApJ, 623, 585
Fortney, J. J., Marley, M. S., & Barnes, J. W. 2007, ApJ, 659, 1661
Hinz, P., Arbo, P., Bailey, V., Connors, T., Durney, O., Esposito, S., Hoffmann, W., Jones, T., Leisenring, J., Montoya, M., Nash, M., Nelson, M., McMahon, T., Pinna, E., Puglisi, A., Skemer, A., Skrutskie, M., & Vaitheeswaran, V. 2012, in Society of Photo-Optical Instrumentation Engineers (SPIE) Conference Series, Vol. 8445, Society of Photo-Optical Instrumentation Engineers (SPIE) Conference Series
Hori, Y. & Ikoma, M. 2011, MNRAS, 416, 1419
Hubickyj, O., Bodenheimer, P., & Lissauer, J. J. 2005, Icarus, 179, 415
Ikoma, M., Nakazawa, K., & Emori, H. 2000, ApJ, 537, 1013
Kenyon, S. J. & Bromley, B. C. 2009, ApJ, 690, L140
Kippenhahn, R. & Weigert, A. 1990, Stellar Structure and Evolution
Kratter, K. M., Murray-Clay, R. A., & Youdin, A. N. 2010, ApJ, 710, 1375
Lagrange, A.-M., Bonnefoy, M., Chauvin, G., Apai, D., Ehrenreich, D., Boccaletti, A., Gratadour, D., Rouan, D., Mouillet, D., Lacour, S., & Kasper, M. 2010, Science, 329, 57
Lambrechts, M. & Johansen, A. 2012, A&A, 544, A32

Lissauer, J. J., Hubickyj, O., D'Angelo, G., & Bodenheimer, P. 2009, Icarus, 199, 338
Macintosh, B. A., Anthony, A., Atwood, J., Barriga, N., Bauman, B., Caputa, K., Chilcote, J., Dillon, D., Doyon, R., Dunn, J., Gavel, D. T., Galvez, R., Goodsell, S. J., Graham, J. R., Hartung, M., Isaacs, J., Kerley, D., Konopacky, Q., Labrie, K., Larkin, J. E., Maire, J., Marois, C., Millar-Blanchaer, M., Nunez, A., Oppenheimer, B. R., Palmer, D. W., Pazder, J., Perrin, M., Poyneer, L. A., Quirez, C., Rantakyro, F., Reshtov, V., Saddlemyer, L., Sadakuni, N., Savransky, D., Sivaramakrishnan, A., Smith, M., Soummer, R., Thomas, S., Wallace, J. K., Weiss, J., & Wiktorowicz, S. 2012, in Society of Photo-Optical Instrumentation Engineers (SPIE) Conference Series, Vol. 8446, Society of Photo-Optical Instrumentation Engineers (SPIE) Conference Series
Marleau, G.-D. & Cumming, A. 2013, arXiv:1302.1517
Marois, C., Macintosh, B., Barman, T., Zuckerman, B., Song, I., Patience, J., Lafrenière, D., & Doyon, R. 2008, Science, 322, 1348
Matzner, C. D. & Levin, Y. 2005, ApJ, 628, 817
Menou, K. & Goodman, J. 2004, ApJ, 606, 520
Mizuno, H., Nakazawa, K., & Hayashi, C. 1978, Progress of Theoretical Physics, 60, 699
Ormel, C. W. 2013, MNRAS, 428, 3526
Papaloizou, J. C. B. & Nelson, R. P. 2005, A&A, 433, 247
Papaloizou, J. C. B. & Terquem, C. 1999, ApJ, 521, 823
Perri, F. & Cameron, A. G. W. 1974, Icarus, 22, 416
Podolak, M. 2003, Icarus, 165, 428
Pollack, J. B., Hubickyj, O., Bodenheimer, P., Lissauer, J. J., Podolak, M., & Greenzweig, Y. 1996, Icarus, 124, 62
Rafikov, R. R. 2005, ApJ, 621, L69
—. 2006, ApJ, 648, 666
—. 2011, ApJ, 727, 86
Saumon, D., Chabrier, G., & van Horn, H. M. 1995, ApJS, 99, 713
Semenov, D., Henning, T., Helling, C., Ilgner, M., & Sedlmayr, E. 2003, A&A, 410, 611
Stevenson, D. J. 1982, Planet. Space Sci., 30, 755
Williams, J. P. & Cieza, L. A. 2011, ARA&A, 49, 67
Youdin, A. N. & Kenyon, S. J. From Disks to Planets, ed. T. D. Oswalt, L. M. French, & P. Kalas, 1
Youdin, A. N. & Mitchell, J. L. 2010, ApJ, 721, 1113
Zhu, Z., Stone, J. M., & Rafikov, R. R. 2013, ApJ, 768, 143

APPENDIX

A. DERIVATION OF THE GLOBAL ENERGY EQUATION

To derive the global energy equation (16) for an embedded protoplanet, we generalize the analogous calculations in stellar structure theory, e.g. in §4.3 of Kippenhahn & Weigert (1990). For our problem, we add the effects of finite core radius, surface pressure and mass accretion. We start with the local energy equation (10d), whose more natural form in Lagrangian (mass) coordinates is $\partial L/\partial m = \epsilon - T\partial S/\partial t$. Integrating from the core to a higher shell with enclosed mass M gives:

$$L - L_{\rm c} = \int_{M_{\rm c}}^{M} \frac{\partial L}{\partial m} dm \tag{A1a}$$

$$= \int_{M_{\rm c}}^{M} \left(\epsilon - T\frac{\partial S}{\partial t}\right) dm \tag{A1b}$$

$$= \Gamma - \int_{M_c}^{M} \frac{\partial u}{\partial t} dm + \int_{M_c}^{M} \frac{P}{\rho^2} \frac{\partial \rho}{\partial t} dm, \tag{A1c}$$

with $\Gamma = \int \epsilon\, dm$ the integral of the direct heating rate, and applying the first law of thermodynamics in the final step.

The global energy equation is derived by eliminating the partial time derivatives in Equation (A1c), which are performed at a fixed mass, in favor of total time derivatives, denoted with overdots. For instance, the surface radius R of the shell with enclosed mass M evolves as

$$\dot{R} = \frac{\partial R}{\partial t} + \frac{\dot{M}}{4\pi R^2 \rho_M}, \tag{A2}$$

where $\partial R/\partial t$ gives the Lagrangian contraction of the "original" shell, and mass accretion through the upper boundary at rate $\dot{M}$ also changes the shell location. Similarly, the volume $V = (4\pi/3)R^3$ and pressure at the outer shell evolve

as

$$\dot{V}_M = \frac{\partial V_M}{\partial t} + \frac{\dot{M}}{\rho_M} \tag{A3a}$$

$$\dot{P}_M = \frac{\partial P_M}{\partial t} + \frac{\partial P_M}{\partial m}\dot{M} = \frac{\partial P_M}{\partial t} - \frac{GM}{4\pi R^4}\dot{M}. \tag{A3b}$$

This derivation holds the core mass and radius fixed, $\dot{M}_\mathrm{c} = \dot{R}_\mathrm{c} = 0$. Therefore, the core pressure satisfies

$$\dot{P}_\mathrm{c} = \partial P_\mathrm{c}/\partial t. \tag{A4}$$

The internal energy integral follows simply from Leibniz's rule as

$$\int_{M_\mathrm{c}}^{M(t)} \frac{\partial u}{\partial t}dm = \dot{U} - \dot{M}u_M. \tag{A5}$$

To make further progress, we use the virial theorem:

$$E_G = -3\int_{M_\mathrm{c}}^{M} \frac{P}{\rho}dm + 4\pi(R^3 P_M - R_\mathrm{c}^3 P_\mathrm{c}), \tag{A6}$$

which follows from Equations (10a), (10b) and (14) by integrating hydrostatic balance in Lagrangian coordinates. As an aside, the integral in equation (A6) can be evaluated for a polytropic EOS to give simple expressions for the total energy:

$$E = (1-\zeta)U + 4\pi(R^3 P_M - R_\mathrm{c}^3 P_\mathrm{c}) \tag{A7a}$$

$$= \frac{\zeta-1}{\zeta}E_G + \frac{4\pi}{\zeta}(R^3 P_M - R_\mathrm{c}^3 P_\mathrm{c}), \tag{A7b}$$

where $\zeta \equiv 3(\gamma-1)$. We will not make this assumption and will keep the EOS general.

To express the work integral, i.e. the final term in Equation (A1c), in terms of changes to gravitational energy, we first take the time derivative of Equation (A6):

$$\dot{E}_G = 3\int_{M_\mathrm{c}}^{M} \frac{P}{\rho^2}\frac{\partial \rho}{\partial t}dm - 3\int_{M_\mathrm{c}}^{M} \frac{\partial P}{\partial t}\frac{dm}{\rho} - 3\frac{P_M}{\rho_M}\dot{M} + 3\dot{P}_M V_M - 3\dot{P}_\mathrm{c}V_\mathrm{c} + 3P_M\dot{V}_M. \tag{A8}$$

The first integral in Equation (A8) is the one we want, but the second one must be eliminated. The time derivative of Equation (14) (times four) gives

$$4\dot{E}_G = -4\frac{GM\dot{M}}{R} + 4\int_{M_\mathrm{c}}^{M} \frac{Gm}{r^2}\frac{\partial r}{\partial t}dm \tag{A9a}$$

$$= -4\frac{GM\dot{M}}{R} + 4\pi\int_{M_\mathrm{c}}^{M} r^3 \frac{\partial}{\partial m}\frac{\partial P}{\partial t}dm \tag{A9b}$$

$$= -4\frac{GM\dot{M}}{R} - 3\int_{M_\mathrm{c}}^{M} \frac{\partial P}{\partial t}\frac{dm}{\rho} + 3V_M\frac{\partial P_M}{\partial t} - 3V_\mathrm{c}\frac{\partial P_\mathrm{c}}{\partial t}, \tag{A9c}$$

where Equations (A9b) and (A9c) use hydrostatic balance and integration by parts.

Subtracting Equations (A5) and (A9c) and rearranging terms with the help of Equations (A2), (A3) and (A4) gives

$$\int_{M_\mathrm{c}}^{M} \frac{P}{\rho^2}\frac{\partial \rho}{\partial t}dm = -\dot{E}_G - \frac{GM\dot{M}}{R} - P_M\frac{\partial V_M}{\partial t}. \tag{A10}$$

Combining Equations (A1c), (A5) and (A10), we reproduce Equation (16) with the accreted specific energy $e_M \equiv u_M - GM/R$.

B. ANALYTIC COOLING MODEL DETAILS

B.1. *Isothermal Atmosphere*

We consider the structure of a non-self-gravitating, isothermal atmosphere that extends outward from the radiative-convective boundary (RCB) and matches onto the disk density, ρ_d, at a distance $r_\mathrm{fit} = n_\mathrm{fit}R_\mathrm{B}$, where R_B is the Bondi radius defined in equation (7). From equation (10b) the resulting density profile is

$$\rho = \rho_\mathrm{d}\exp\left(\frac{R_\mathrm{B}}{r} - \frac{1}{n_\mathrm{fit}}\right) \approx \rho_\mathrm{d}\exp\left(\frac{R_\mathrm{B}}{r}\right), \tag{B1}$$

where the approximate inequality is valid deep inside the atmosphere ($r \ll R_{\mathrm{B}}$) for any $n_{\mathrm{fit}} \gtrsim 1$. However, the choice of boundary condition does have an order unity effect on the density near the Bondi radius.

The mass of the atmosphere is determined by integrating equation (10a) from the RCB to the Bondi radius using the density profile (B1) and can be approximated as

$$M_{\mathrm{iso}} \approx 4\pi \rho_{\mathrm{d}} \frac{R_{\mathrm{RCB}}^4}{R_{\mathrm{B}}} e^{R_B/R_{\mathrm{RCB}}} = 4\pi \rho_{\mathrm{RCB}} \frac{R_{\mathrm{RCB}}^4}{R_{\mathrm{B}}}\,, \tag{B2}$$

with ρ_{RCB} the density at the RCB. This result is the leading order term in a series expansion. By comparing the expression above and Equation (26) under the assumption that $R_{\mathrm{RCB}} \ll R_{\mathrm{B}}$, we see that the mass of the outer radiative region (which is nearly isothermal) is negligible when compared with the atmosphere mass in the convective layer, as stated in Section 3.

B.2. *Temperature and Pressure Corrections at the Radiative-Convective Boundary*

We estimate the temperature and pressure corrections at the RCB due to the fact that the radiative region is not purely isothermal. From equation (11), we express the radiative lapse rate

$$\nabla_{\mathrm{rad}} = \frac{3\kappa P}{64\pi G M \sigma T^4} L = \nabla_{\mathrm{d}} \frac{P/P_{\mathrm{d}}}{(T/T_{\mathrm{d}})^{4-\beta}}\,, \tag{B3}$$

where the second equality follows from the opacity law (5) and ∇_{d} is the radiative temperature gradient at the disk:

$$\nabla_{\mathrm{d}} \equiv \frac{3\kappa(T_{\mathrm{d}})P_{\mathrm{d}}}{64\pi G M \sigma T_{\mathrm{d}}^4} L. \tag{B4}$$

Here M is the total planet mass. Since our analytic model neglects self-gravity, $M = M_{\mathrm{c}}$ and therefore ∇_{d} is constant. From equation (B3) and $\nabla_{\mathrm{rad}} = d\ln T/d\ln P$, the temperature profile in the radiative region integrates to

$$\left(\frac{T}{T_{\mathrm{d}}}\right)^{4-\beta} - 1 = \frac{\nabla_{\mathrm{d}}}{\nabla_{\infty}}\left(\frac{P}{P_{\mathrm{d}}} - 1\right)\,, \tag{B5}$$

where $\nabla_{\infty} = 1/(4-\beta)$ is the radiative temperature gradient for $T, P \to \infty$. Applying Equations (B3) and (B5) at the RCB (where $\nabla_{\mathrm{rad}} = \nabla_{\mathrm{ad}}$) under the assumption that $P_{\mathrm{RCB}} \gg P_{\mathrm{d}}$ results in $T_{\mathrm{RCB}} = \chi T_{\mathrm{d}}$ as in Equation (19a), with χ defined in Equation (20).

The pressure at the RCB follows from Equations (B5) and (19a) as

$$\frac{P_{\mathrm{RCB}}}{P_{\mathrm{d}}} \simeq \frac{\nabla_{\mathrm{ad}}/\nabla_{\mathrm{d}}}{1 - \nabla_{\mathrm{ad}}/\nabla_{\infty}}. \tag{B6}$$

We can eliminate ∇_{d} from equation (B6) to obtain a relation between temperature and pressure in the radiative zone as a function of the RCB pressure P_{RCB}. From Equation (B5), it follows that

$$\frac{T}{T_{\mathrm{d}}} = \left[1 + \frac{1}{\frac{\nabla_{\infty}}{\nabla_{\mathrm{ad}}} - 1}\left(\frac{P}{P_{\mathrm{RCB}}} - \frac{P_{\mathrm{d}}}{P_{\mathrm{RCB}}}\right)\right]^{\frac{1}{4-\beta}}. \tag{B7}$$

We can then determine the RCB radius R_{RCB} from Equation (10b) as

$$\frac{R_B}{R_{\mathrm{RCB}}} = \int_{P_{\mathrm{d}}}^{P_{\mathrm{RCB}}} \frac{T}{T_{\mathrm{d}}} \frac{dP}{P}\,. \tag{B8}$$

Evaluating the integral leads to

$$\frac{R_B}{r_{\mathrm{RCB}}} = \ln\left(\frac{P_{\mathrm{RCB}}}{P_{\mathrm{d}}}\right) - \ln\theta\,, \tag{B9}$$

with an extra correction term $\theta < 1$, when compared to an isothermal atmosphere (see Equation B1). From this we arrive at the relation between P_{RCB} and P_{d} given by Equation (19b). As opposed from the temperature correction factor χ, an analytic expression for θ cannot be obtained. Estimates for χ and θ for different values of the exponent β in the opacity law (5) are presented in Table 1.

B.3. *The Opacity Effect*

A lower opacity decreases the critical core mass. Reducing the opacity by a factor of one hundred results in a critical core mass one order of magnitude lower than in the standard ISM case, for our analytic model. The reduction is not as strong as the nominal scaling would imply, $0.01^{3/5} \approx 0.06$, because ξ increases.

TABLE 1
PARAMETERS DESCRIBING STRUCTURE OF RADIATIVE ZONE.

$\gamma = 7/5$ ($\nabla_{\mathrm{ad}} = 2/7$)				
β	1/2	3/4	1	3/2	2
∇_∞	2/7 [a]	4/13	1/3	2/5	1/2
χ	$\cdots$	2.25245	1.91293	1.65054	1.52753
θ	$\cdots$	0.145032	0.285824	0.456333	0.556069

[a] Since $\nabla_{\mathrm{ad}} = \nabla_\infty$ there is no convective transition at depth for this case.

Even with significantly lower opacities, radiative diffusion remains a good approximation at the RCB. For $\beta = 2$, we estimate the optical depth as

$$\tau_{\mathrm{RCB}} \sim \frac{\kappa_{\mathrm{RCB}} P_{\mathrm{RCB}}}{g} \sim 7 \times 10^4 \frac{F_T^4 F_\kappa}{\left(\frac{m_{\mathrm{c}\oplus}}{10}\right)\left(\frac{a_\oplus}{10}\right)^{\frac{12}{7}}}, \tag{B10}$$

where $P_{\mathrm{RCB}} \sim P_M$ for a self-gravitating atmosphere and $g \sim GM_{\mathrm{c}}/R_B^2$, with both approximations good to within the order unity factor ξ. We see that $\tau_{\mathrm{RCB}} \gg 1$ even for $F_\kappa \lesssim 0.01$ out to very wide separations, hence the atmosphere remains optically thick at the RCB.

B.4. Surface Terms

In this section we check the relevance of the neglected surface terms in Equation (16). We first show that accretion energy is only a small correction at the RCB, which is where we apply our cooling model. A rough comparison (ignoring terms of order ξ) of accretion luminosity vs. $\dot{E}$ gives

$$\frac{GM\dot{M}}{R\dot{E}} = \frac{GM}{R}\frac{dM}{dE} \sim \frac{GM_{\mathrm{c}}^2}{R_B E}\frac{P_{\mathrm{RCB}}}{P_M} \sim \sqrt{\frac{R_{\mathrm{c}}}{R_B}} \ll 1, \tag{B11}$$

where we assume $P_{\mathrm{RCB}} \sim P_M$ for a massive atmosphere. Accretion energy at the protoplanetary surface is thus very weak for marginally self-gravitating atmospheres, and even weaker for lower mass atmospheres. A similar scaling analysis shows that the work term $P_M \partial V_M/\partial t$ is similarly weak. Nevertheless, our numerical calculations include these surface terms in a more realistic and complete model of self-gravitating atmospheres.